Ultra-broadband perfect absorption based on MXene metamaterial for visible light to mid-infrared solar energy harvesting

S. XIONG[1], Y. PAN[2], F. CHEN[2,*]
[1]*Yangtze University College of Arts and Science, Jingzhou 434023, China*
[2]*School of Physics and Optoelectronic Engineering, Yangtze University, Jingzhou, 434023, China*

In the work, we design and propose an ultra-broadband solar energy absorber based on $MXene$ metamaterial. The proposed pyramid structure is formed by five layers $MXene-SiO_2$ of a stacking. The average absorption across the range of 300-2616 nm is 98.83%. The physical mechanism is illustrated by electric field and magnetic field distributions, including the dielectric lossy property of $MXene$ itself in shorter wavelengths, Fabry-Perot (FP) resonance, and local surface plasmon resonance (LSPR) in longer wavelengths. The result indicates that the energy absorption spectrum can be well matched with the standard solar spectrum under AM 1.5 over the full range of 300 to 2700 nm, wiht only 1.18% loss. Ultimately, the influence of different materials and geometrical parameters on absorption is investigated. The absorber can achieve ultra-broadband perfect absorption, and has a simple structure that is easy to manufacture. The result of this work can be applied in many potential fields, such as thermal photovoltaic power generation, infrared imaging, solar cells, and other optoelectronic devices.

(Received February 10, 2025; accepted October 14, 2025)

Keywords: MXenes, Perfect absorption, Metamaterials, Electromagnetic simulation

1. Introduction

Broadband absorption in the solar spectrum (300-2500 nm) is critical for solar cell technology because it is what makes them functional [1-3]. A lot of different devices have been proposed, such as solar cells, solar collectors, and thermoelectric devices [4-9]. Wide-band solar absorbers have attracted considerable attention [10-12]. Traditional film-based absorbers are appropriate for large-scale manufacturing; nevertheless, their multilayer configurations result in intricate and time-intensive design and production processes [13, 14]. In addition, wide-band solar absorber typically features both planner and vertical structures. By strategically placing resonators of varying shapes, planar designs aim to absorb a wide range of wavelengths [15, 16] while vertical structures are prevalent in wide-band absorption, involving the stacking of multilayer structures in a vertical orientation. This configuration achieves broadband absorption through the layering of many films or by creating an embedded structure with the upper and lower layers [17].

The phenomenal and peculiar features of metamaterials have attracted a lot of interest over the past two decades. Because of these characteristics, electromagnetic waves may be controlled at the subwavelength scale of the incident light [18, 19]. Metamaterials and metasurfaces are a class of artificial materials whose electromagnetic behavior is governed not by their composition but by the size of their meta-atoms or unit cells [20-24]. Flat lenses [25], imaging [26], nano-antennas [27], sensors [28], Bessel beam production [29], energy harvesters [30], plasmon-induced transparency [31, 32], and absorbers [33] are only a part of optical and photonic devices and systems that utilize metamaterials. Recent advancements in optical devices utilizing metamaterials have not only expanded their applications in optical communications and imaging [34] but also introduced new opportunities for the development of broadband solar spectrum absorption.

In recent times, the scientific community has shown significant interest in a novel substance known as $MXene$, owing to its notable attributes like better tunability and exceptional thermal handling, rendering it suitable for applications such as absorbers and solar energy systems [35, 36]. $MXene$ has remarkable conductivity, making it particularly useful for various electrical and optoelectronic applications. The remarkable surface area of $MXene$ is attributed to its two-dimensional (2D) arrangement, which finds optimal utilization in many applications such as sensing and energy storage. Until now, only a limited number of studies have explored $MXene$-based nano-absorbers.

For example, a broadband plasmonic *MXene*-based absorber is investigated which showed an absorption value (80–90%) from 550 to 2100 nm [37]. Moreover, another ultrawideband absorber which is composed of nanospheres of *MXene* and *W* is presented which covers the ultraviolet to infrared region from 400 to 2500 nm with an average absorption of 95 % [38]. Likewise, a multilayer plasmonic absorber is also explored which is composed of a multilayer of $MXene-SiO_2$ and showed a large optical absorption bandwidth from 400 to 2000 nm [39]. The existing *MXene*-based absorbers contain good absorption bandwidth and they also use multilayered design configuration. Consequently, *MXene* holds significant potential in the development of plasmonic absorbers, particularly in enhancing absorption bandwidth with single-layer design topologies. This advancement has diverse applications, including solar photovoltaics and energy harvesting.

In the paper, we design an ultra-broadband solar absorber. It consists of five layers $MXene-SiO_2$ stacked on a *Fe* substrate. We calculate the absorption spectrum of the absorber. By analyzing the electric fields and magnetic fields, we explain the physical mechanism of the high absorption performance. Then the solar energy absorption ability is investigated by comparing the solar absorption with the standard solar spectrum under AM1.5. Further, the absorption properties of different structures are compared. We believe that this absorber possesses satisfactory application in the solar energy collection field. This work has great potential for applications in solar energy collection devices, thermoelectric radiation, photovoltaics, and other optoelectronic devices.

2. Model and theory

A three-dimensional structure schematic of the ultra-wideband absorber is shown in Fig. 1(a). The unit cell consists of five pairs of $MXene/SiO_2$. The areas of composite layers are decreased from top to bottom. They are placed on the Fe substrate and spread in both the x- and y-directions. The red and blue layers represent *MXene* and SiO_2, respectively. The structure parameters of each part are exhibited in Fig. 1(b). Every layer of *MXene* has the same thickness $t_1 = 30\,nm$, and every layer of SiO_2 has the same thickness $t_2 = 60\,nm$. A rectangular layer is formed by combining one layer of *MXene* and one layer of SiO_2. The width of each rectangular layer in the x- and y-directions is the same. The widths increase gradually from top to bottom, which are $w_1 = 60\,nm$, $w_2 = 120\,nm$, $w_3 = 190\,nm$, $w_4 = 220\,nm$, and $P = 280\,nm$. The dielectric constant of SiO_2 is set as 1.46 [40]. The dielectric constants of *Fe* is referred to the experimental values of Palik [41]. The substrate is served as by *Fe* and is 300 nm thick. Consequently, the substrate's thick base layer ensures that the light transmittance is zero ($T = 0$), so the absorbance $A = 1 - R$, and R represents the reflectance of the structure. The permittivity of *MXene* was fitted using the Drude-Lorentz model with the following equation [42]:

$$\varepsilon_{Drude} = \varepsilon_{f_1} - (\frac{\omega_p}{\omega})^2 + i(\varepsilon_{f_2} + \frac{\omega_p^2 \gamma}{\omega^3 + \omega\gamma^2}) \quad (1)$$

$$\varepsilon_{Lorentz} = \varepsilon_{f_3}\left[1 + \frac{\omega_p^2(\omega_0^2 - \omega^2) + i\omega_0^2\gamma\omega}{(\omega_0^2 - \omega^2) + \gamma^2\omega^2}\right] \quad (2)$$

Here, the plasma frequency of the $Ti_3C_2T_x$ was $\omega_p = 4.21\times10^{15}$ rad/s, the dispersion losses were $\gamma = 8.65\times10^{14}$ rad/s, the Lorentz pole frequency $\omega_0 = 2.301\times10^{15}$ rad/s, and fitting parameters were $\varepsilon_{f_1} = 6.0$ $\varepsilon_{f_2} = 3.0$ $\varepsilon_{f_3} = 0.2$. The FDTD method is employed in this study to determine the absorber's absorption characteristics. After that, it is investigated how physical parameters affect absorption performance, and the physical process of ultra-wideband absorption is investigated in combination with electromagnetic theory in order to give theoretical direction for the design of ultra-wideband absorbers. The total simulation region is $280\times280\times5000\,nm$. The conditions for the boundary in the x- and y- direction are set as periodic boundaries, and the boundary condition in the z direction is perfectly matching layer (PML). During the simulation, the mesh size is $5\times5\times2\,nm$ in x-, y- and z-directions, respectively. The light source is a plane wave light source. For TM and TE polarization lights, the absorption spectra are equal owing to the symmetrical structure. Therefore, only TM polarization is considered here. The wavelength of the source is range from $300\,nm$ to $2700\,nm$.

Fabrication involves depositing MXene/ SiO_2 layers via dual-gun RF sputtering or e-beam evaporationonto the Fe substrate, followed by precision etching (e.g., focused ion beam lithography) to achieve

the pyramidal geometry. Key advantages include polarization/angular insensitivity (maintaining >80% absorption up to 60° incidence), minimal solar energy loss (1.18% under AM 1.5), and scalability over complex planar designs. Material selection is critical—MXene provides superior conductivity and plasmonic tunability, while SiO_2 optimizes FP resonance—with experimental validation showing outperformance over Au, Al, Al_2O_3, and Si_3N_4 alternatives.

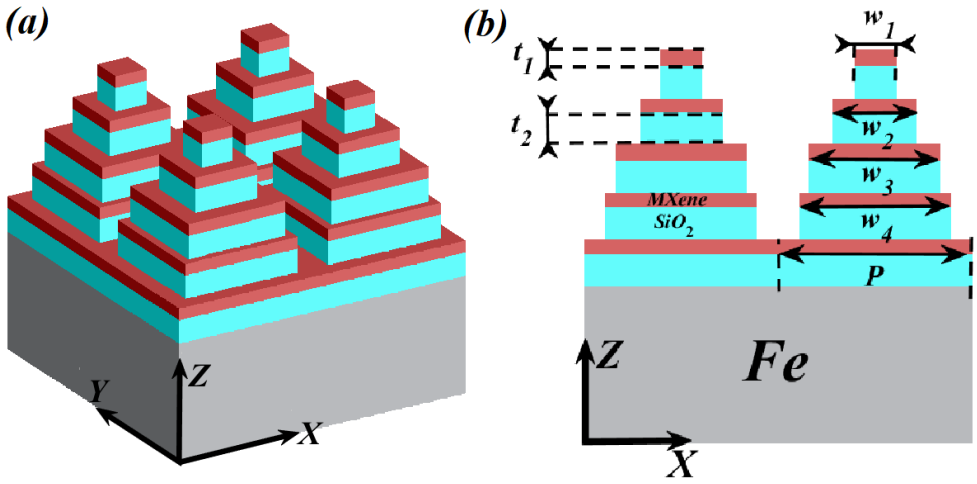

Fig. 1. (a) Three-dimension structure diagram of the proposed broadband absorber. (b) The side view of the proposed absorber (colour online)

3. Results and discussion

The proposed structure can achieve super absorption, as shown in Fig. 2. It can be noticed four absorption peaks located at 382 nm, 660 nm, 1282 nm, and 2177 nm, and the absorption is about 99.84%, 99.96%, 99.98%, and 98.85%, respectively. The absorption bandwidth is up to 2316 nm (over 90%) from 300 nm to 2616 nm. The average efficiency of absorption bandwidth is 98.83%. In Table 1, compared with other broadband absorbers [43-47], this absorber has the largest average absorption efficiency and a relatively excellent absorption bandwidth.

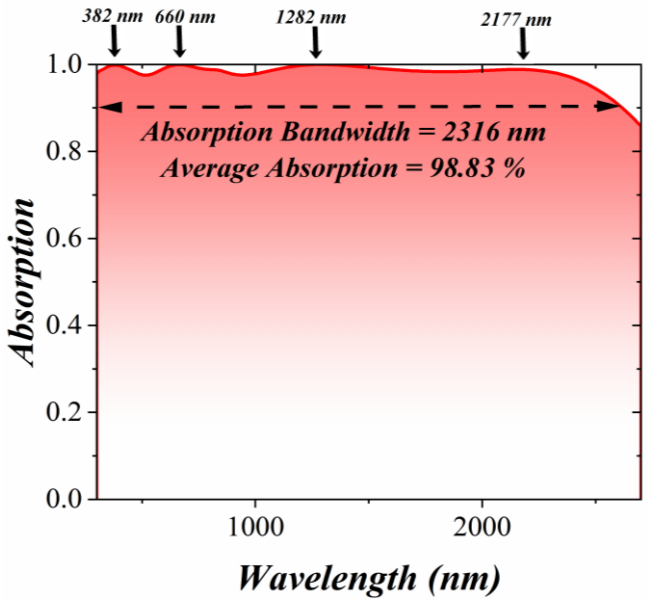

Fig. 2. The absorption spectrum of the proposed structure (colour online)

Table 1. Comparison between proposed structure and other absorber

Ref.	Year	Material	Average Absorption	Absorption Bandwidth
[43]	2025	*MXene*	97.3 %	2882 nm
[44]	2025	*MXene* / *W*	> 95 %	2041 nm
[45]	2024	*Ti* / Al_2O_3 / *MXene* / SiO_2	97.6 %	1200 nm
[46]	2023	*MXene* / *AlN*	90 %	1800 nm
[47]	2024	*MXene* / *AlN*	> 90 %	2000 nm
This work	2025	*MXene* / SiO_2 / *Fe*	98.8 %	2316 nm

To study and explain the physical mechanism of the absorber, the electric and magnetic field distributions in X-Z plane are shown in Fig. 3(a)-(h). Obviously, the local field indicates that the surface plasmon is excited here, causing almost perfect absorption in the full wavelength. At a wavelength of 382 nm, the electric field is primarily concentrated on the edge of the fourth and fifth layer *MXene*. The magnetic field is mainly distributed on the SiO_2 layer. This indicates that the coupling between the electromagnetic wave and the $MXene-SiO_2$ layer leads to FP cavity resonance and the excitation of LSPR [48-50]. At a wavelength of 660 nm, the electric field is mainly concentrated on the edge of the fourth and fifth layer *MXene*. The magnetic field is distributed at the upper surface of the third, fourth, and fifth SiO_2 layer, with some presence at the interface between the *Fe* substrate and the SiO_2 layer. Therefore, the strong absorption at this wavelength results from the combined effects of LSPR, and FP cavity resonance [51-53]. At a wavelength of 1282 nm, the electric field is distributed on both sides of each layer *MXene*. The magnetic field is localized on the lower surface of the fifth SiO_2 layer. The strong absorption in this band is attributed to the combined effects of cavity mode resonance and the excitation of LSPR. At a wavelength of 2177 nm, the electric field is mainly concentrated on the gap between unit cells. The magnetic field is concentrated within the second, third, and fourth SiO_2 layer and at the interface between the SiO_2 and *MXene* layers. This indicates that at this wavelength, both the FP cavity and LSPR are excited, with the modes coupling to reduce reflection. As a result, the strong absorption at this wavelength is due to the combined effects of LSPR and FP cavity resonance.

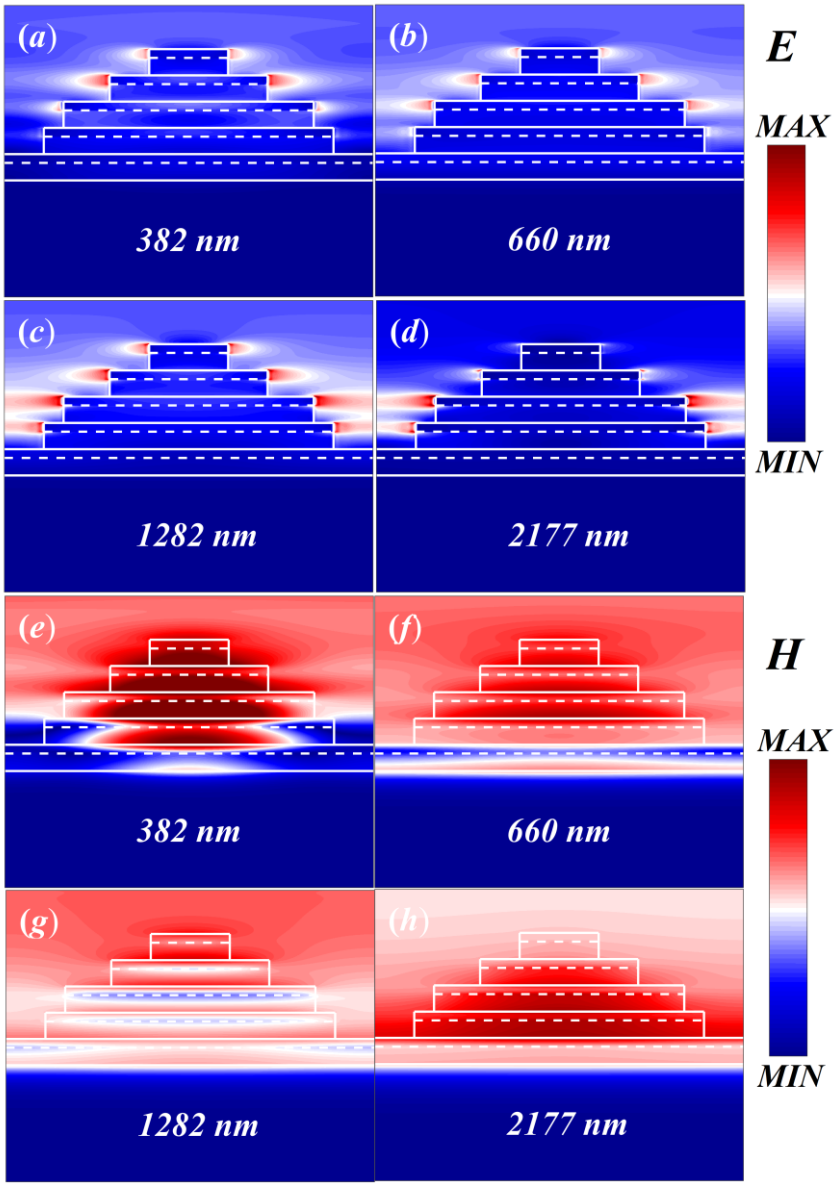

Fig. 3. (a)-(d) The electric field distribution in the X-Z plane at different wavelengths; (e)-(h) The magnetic field distribution in the X-Z plane at different wavelengths (colour online)

The light source usually cannot incident perpendicular to the device. In practical applications, we must take into account the influence of solar incidence angle. Therefore, it is necessary to study solar absorbers that highly include light incidence angles. In Fig. 4, the influence of the incident angle and polarization angle of the structure is shown. Fig. 4(a) exhibits the relationship between the polarization angle and the absorption. When the polarization angle increases from 0° to 90°, the absorption is almost unchanged, this is because the proposed structure is geometric symmetry. Fig. 4(b) shows the spectral absorption performance of the absorber under TM polarization, and Fig. 4(c) exhibits the spectral absorption under TE wave incidence from 0° to 70°, we can notice that when the incident angle is increased, the absorption band shows a slight changes. But the absorption band only changes slightly. This indicates that the absorber has high angular stability.

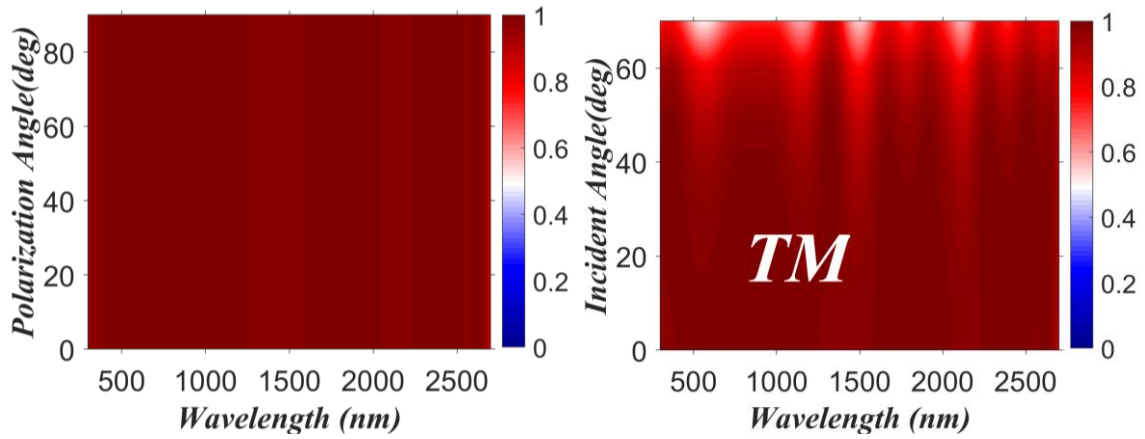

(a) (b)

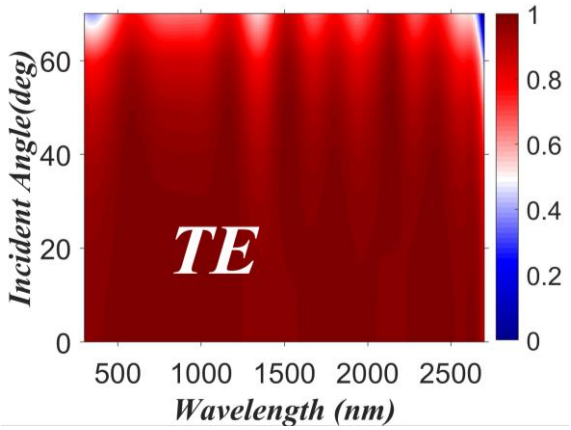

(c)

Fig. 4. (a) The absorption spectra with different polarization angles. (b) The absorption spectra with different incident angles under TM polarized. (c) The absorption spectra with different incident angles under TE polarize (colour online)

The influence of the number of $MXene-SiO_2$ layers on the absorption spectrum is investigated, as shown in Fig. 5. When only one $MXene-SiO_2$ layer is used on the Fe substrate, the metamaterial exhibits a relatively low average absorption in the visible to near-infrared range. It reaches an average absorption of 95.14 % from 592.2 to 938.9 nm. However, the absorption bandwidth is narrow. After covering the structure with two layers $MXene-SiO_2$, the absorption bandwidth is increased to 852.7 nm, and an average absorption of 95.51 %. When three layers $MXene-SiO_2$ are used on the Fe substrate, the absorption band is increased clearly. The absorption bandwidth is 2244.7 nm(over 90 %) from 331.3 to 2576 nm. The average absorption is 95.58 %. This result indicates that the addition of the number of $MXene-SiO_2$ layers effectively broaden the width of the high-absorption band. Furthermore, when four $MXene-SiO_2$ layers are added on Fe substrate, the metamaterial achieves near-perfect absorption at multiple wavelengths, with an average absorption exceeding 98.64 % across the full solar spectrum (300-2616 nm). Finally, five $MXene-SiO_2$ layers are fixed on the Fe substrate, and the average absorption rate is raised to 98.83 %.

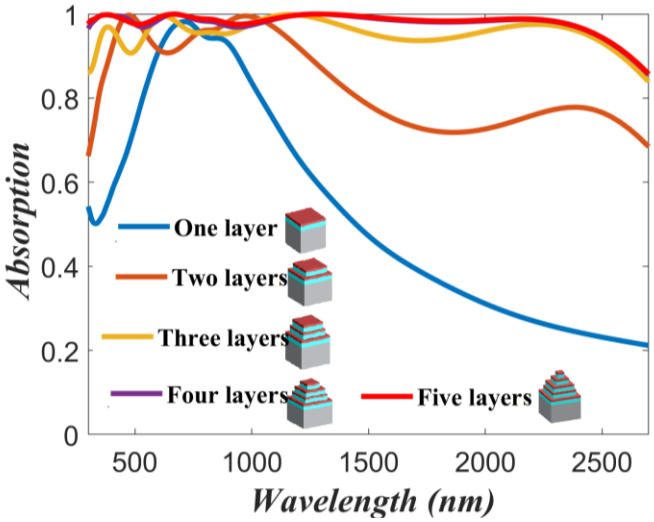

Fig. 5. Comparison of absorption spectra for different layers MXene-SiO_2 (colour online)

In order to investigate the solar energy, absorb efficiency of the proposed absorber, Fig. 6 illustrates the absorption spectrum of the absorber with the sunlight spectrum under AM 1.5. The solar spectral absorption ratio under standard AM1.5 spectral can be expressed as [54, 55]:

$$I_A(\lambda) = A(\lambda) \times I_{AM1.5} \tag{3}$$

$$I_{Loss}(\lambda) = I_{AM1.5}(\lambda) - I_A \tag{4}$$

$$\eta = \frac{\int_{\lambda_{\min}}^{\lambda_{\max}} I_A d\lambda}{\int_{\lambda_{\min}}^{\lambda_{\max}} I_{AM1.5} d\lambda} \tag{5}$$

where λ is the incident light wavelength, $I_{AM1.5}$ is the solar spectra at AM1.5, $I_A(\lambda)$ is the absorbed spectra, and $I_{Loss}(\lambda)$ is the loss solar spectrum. Here, $\lambda_{\min}$, and $\lambda_{\max}$ are 300 nm, and 2700 nm, respectively. Fig. 6(a) presents the comparison between the absorption spectrum of the proposed structure and the standard solar spectrum under AM 1.5. It is observed that the main radiation area of solar energy is distributed in the visible light band and the near-infrared band. The absorption efficiency is 98.82 %. Meanwhile, the absorption spectrum of the absorber is basically consistent with the standard solar spectrum. This indicates the absorber can absorb the solar energy in the full spectrum.

In Fig. 6(b), the energy absorbed, and energy lost are compared. We can see the energy loss is very small. The ratio of energy loss to energy absorption is only 1.18 %, proving the superiority of our design structure. The absorption of the standard solar spectrum under AM 1.5 from one layer $MXene-SiO_2$ to four layers $MXene-SiO_2$ are shown in Fig. 6(c). When one layer $MXene-SiO_2$ is retained, the absorption rate of the structure to the solar spectrum is 77.49 %. When retaining two layers $MXene-SiO_2$, the absorption rate of the structure on the solar spectrum is 92.50 %. When increasing the number of $MXene-SiO_2$ to three, the absorption rate of the structure on the solar spectrum is 96.19 %. Increase the number of $MXene-SiO_2$ layer to four, an absorption rate of 98.83 % for the solar spectrum. Therefore, we choose to cover five layers $MXene-SiO_2$ on the Fe substrate.

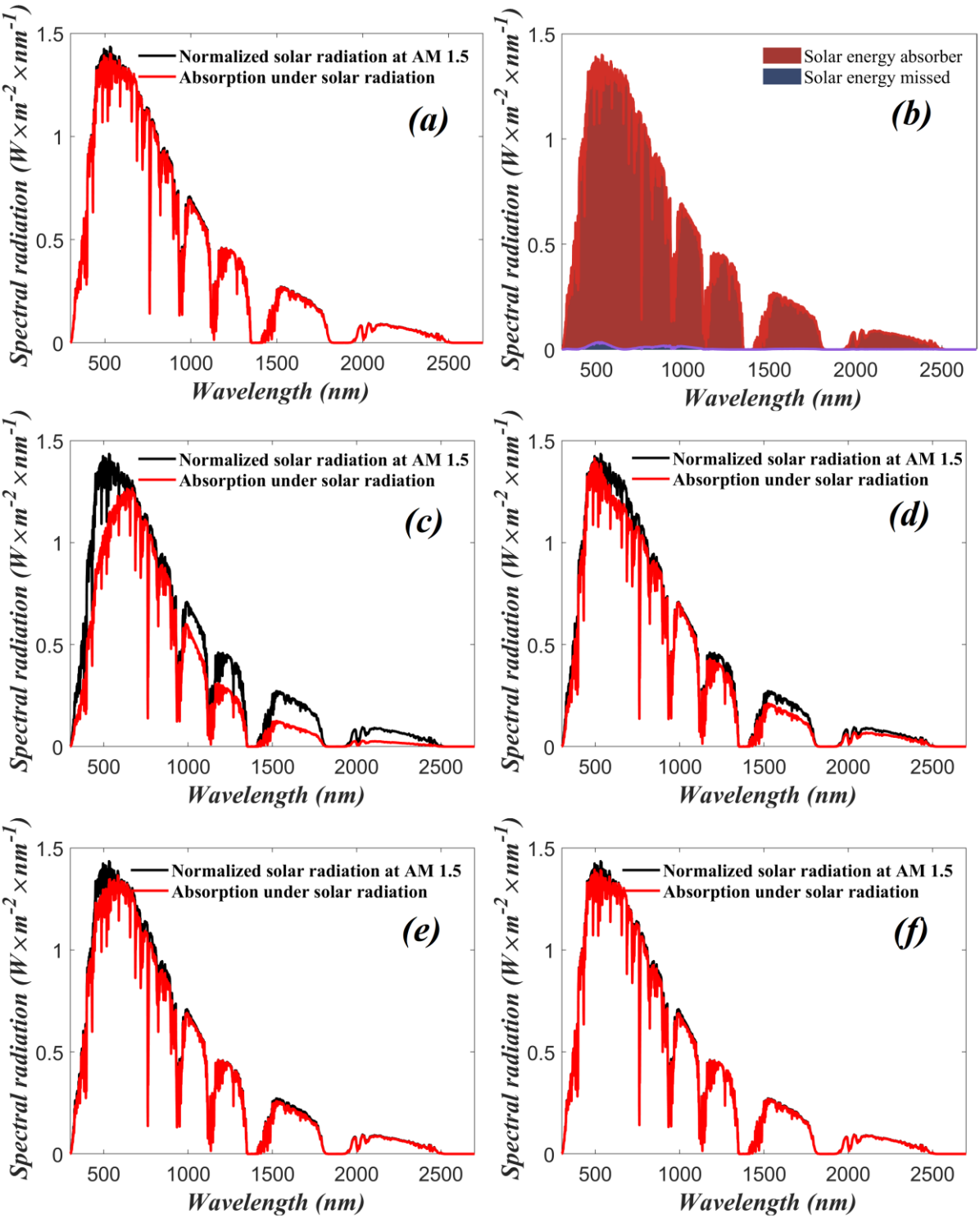

Fig. 6. (a) The comparison between the standard solar spectrum under AM 1.5 and the absorption spectrum of the absorber we proposed (b) The comparison of energy absorbed and energy lost by the absorber. (c)-(f) The comparison between the standard solar spectrum under AM 1.5 and the absorption spectra for different MXene-SiO_2 layers (colour online)

The refractive index sensitivity of the proposed broadband absorber is studied in Fig. 7, when the environment refractive index increases from 1 to 1.3, the absorption width shows a red-shift, this is because the amplitude of plasmon resonance is varied by changing the environment refractive index.

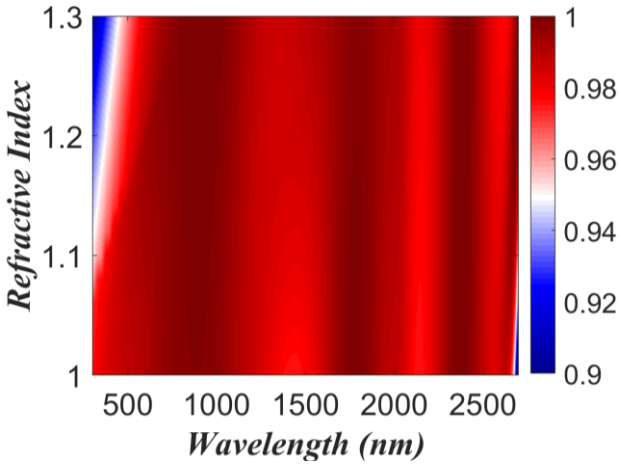

Fig. 7. The relationship between the absorption of the absorber and the background refractive index (colour online)

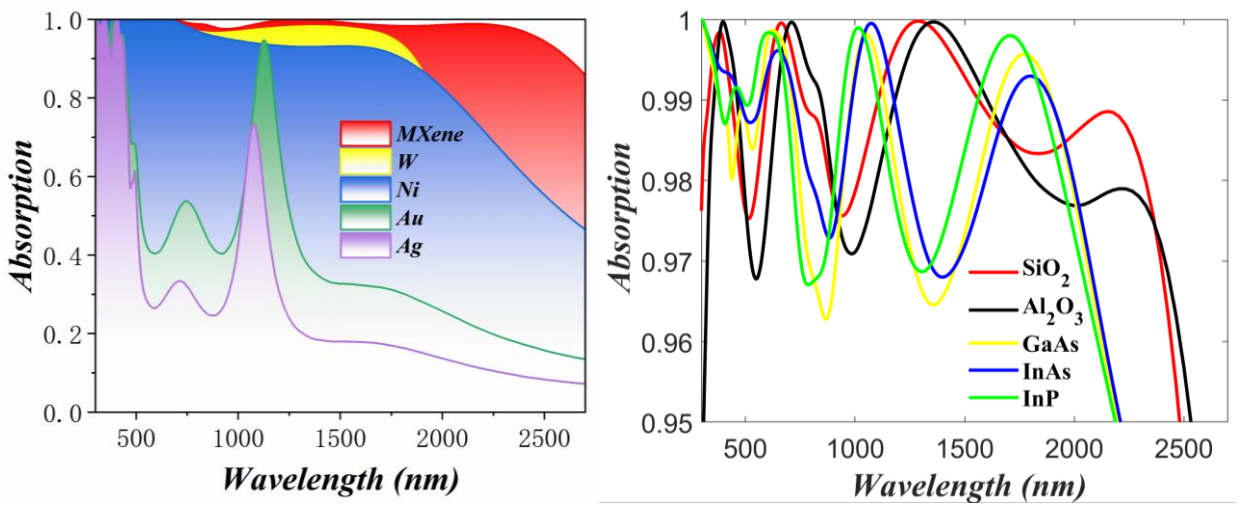

(a) *(b)*

Fig. 8. (a) Absorption diagrams of absorbers with different metal materials. (b) Absorption diagrams of absorbers with different dielectric materials (colour online)

To verify the superiority of *MXene* and SiO_2 in the absorption performance, the absorption spectra with different metals are shown in Fig. 8(a). It is seen that when *MXene* is replaced by W, Ni, Au, and Ag, although some absorption peaks appeared in the spectra, but the absorption peaks are narrow and discontinuous. The refractive indices of W, Ni, Au, and Ag come from Palik [41]. We can see that when using Ag or Au, the average absorption is much lower than the absorption rates of the other three materials. W has better average absorption compared to Ni, but its absorption bandwidth is smaller than that of Ni. *MXene* possesses a best absorption bandwidth and average absorption rate, since *MXene* has a higher dielectric constant in the near-infrared and mid-infrared bands, which can achieve higher and more stable absorption. The study of absorption performance with different dielectrics is shown in Fig. 8(b). The refractive indices of Al_2O_3, $GaAs$, $InAs$, and InP come from Palik [41]. All five materials exhibit good absorption characteristics in the visible-light band. Only SiO_2 achieves the highest average absorption in the operating

band. SiO_2 has the best absorption ability in mid-infrared compared with other dielectric materials.

Recent studies have shown that metamaterial absorbers can be implemented in solar sail applications. NASA has introduced an innovative concept called the Extreme Solar Sail. This cutting-edge technology has the potential to revolutionize space exploration, bringing possibilities for many low-cost and high-speed missions. This proposal marks an important step towards redefining traditional methods of space exploration and expanding the possibilities for future celestial exploration. As a passive propulsion system, solar sails utilize the momentum of solar photons to transfer onto large, highly reflective sails [56]. This study demonstrates the potential application of metamaterial absorbers as solar sails [57]. Inspired by this previous work, the proposed absorber can also be applied to solar sails.

4. Conclusion

In this paper, we proposed a pyramid-shaped structure to achieve ultra-broadband perfect absorption. The absorption spectrum is calculated by the FDTD Solutions. In the ultra-wide spectral range of 2316 nm, the absorption rate is more than 90%, and the average absorption rate is 98.83 %. By analyzing the electric field and magnetic field, we found the dielectric lossy property of *MXene* itself in shorter wavelength, and the Fabry-Perot resonance, and the LSPR in longer wavelength cause strong absorption of light. The perfect absorber exhibits polarization insensitivity under normal incidence. In addition, the absorption rate is higher than 80% with a larger incident angle, which proves the absorber is not sensitive to the angle of incident light. Compared with the standard solar spectrum under AM 1.5, the proposed absorber exhibits a good solar energy collection ability. The absorber can effectively absorb sunlight, and has little energy loss. Different materials have a strong influence on the absorber. It is verified that $MXene$, and SiO_2 have the best performance. By comparing different structures, five layers $MXene-SiO_2$ has the highest absorption level. The absorber in this work can be applied in many potential fields, such as thermal photovoltaic power generation, solar cells, infrared imaging, and other optoelectronic device.

Acknowledgements

Supported by the National Natural Science Foundation of China (Grant No.12075036,12375008). Hubei Provincial Natural Science Foundation Innovation Group Project (Grant No.2023AFA025). The Yangtze University College Students' Innovation and Entrepreneurship (grant No. Yz2024323).

References

[1] W. Zhang, H. Zuo, Z. Cheng, Y. Shi, Z. Guo, N. Meng, Y. Liao, Advanced Materials **34**(18), 2104952 (2022).

[2] J. Bertolotti, Science **377**(6609), 924 (2022).

[3] J. Lord, A. Thomas, N. Treat, M. Forkin, R. Bain, P. Dulac, P. H. Schmaelzle, Nature **598**(7882), 611 (2021).

[4] M. Baeva, D. Gets, A. Polushkin, A. Vorobyov, A. Goltaev, V. Neplokh, S. Makarov, Opto-Electronic Advances **6**, 220154 (2023).

[5] F. Qin, J. Chen, J. Liu, L. Liu, C. Tang, B. Tang, Z. Yi, Solar Energy **262**, 111796 (2023).

[6] J. Maksimovic, J. Hu, S. H. Ng, T. Katkus, G. Seniutinas, T. P. Rivera, S. Juodkazis, Opto-Electronic Advances **5**(9), 210086-1 (2022).

[7] Y. Li, F. Chen, W. Yang, Optics Communications **586**, 131878 (2025).

[8] R. Lin, Y. Wang, Q. Lu, B. Tang, J. Li, H. Gao, H. Tan, Nature **620**(7976), 994 (2023).

[9] L. Wen, L. Zhao, G. Wang, X. Jia, X. Xu, S. Qu, W. Wang, Solar Energy Materials and Solar Cells **258**, 112429 (2023).

[10] B. Cai, L. Wu, X. Zhu, Z. Cheng, Y. Cheng, Results in Physics **58**, 107509 (2024).

[11] L. Wu, L. Yang, B. Cai, Y. Cheng, Z. Cheng, Physica B: Condensed Matter **708**, 417205 (2025).

[12] J. Wang, L. Yang, B. Cai, Y. Cheng, X. Li, Physica E: Low-dimensional Systems and Nanostructures **172**, 116270 (2025).

[13] W. Li, Y. Yi, H. Yang, S. Cheng, W. Yang, H. Zhang, H. Li, Communications in Theoretical Physics **75**(4), 045503 (2023).

[14] Q. Meng, F. Chen, S. Chen, B. Wang, Z. Yi, Physica Scripta **98**(8), 085503 (2023).

[15] Q. Meng, F, Chen, S, Chen, Y. Xu, W. Yang, Z. Yi, Physica Scripta **98**(2), 025511 (2023).

[16] Y. Zhu, P. Cai, W. Zhang, T. Meng, Y. Tang, Z. Yi, Y. Yi, Micromachines **14**(8), 1597 (2023).

[17] J. Liu, C. Dou, W. Chen, W. Z. Ma, D. Meng, X. Q. You, Y. Gu, Solar Energy Materials and Solar Cells **244**, 111822 (2022).

[18] Q. A. Alsulami, S. Wageh, A. A. Al-Ghamdi, R. M. H. Bilal, M. A. Saeed, Polymers **14**(21),

4503 (2022).
[19] R. M. H. Bilal, M. A. Baqir, P. K. Choudhury, M. M. Ali, A. A. Rahim, IEEE Photonics Journal **12**(3), 1 (2020).
[20] X. You, R. T. Ako, S. Sriram, W. Withayachumnankul, Laser and Photonics Reviews **19**(7), 2401011 (2025).
[21] M. Deng, S. Kanwal, Z. Wang, C. Cai, Y. Cheng, J. Guan, L. Chen, Nano Letters **24**(46), 14641 (2024).
[22] Z. Huang, Y. Zheng, J. Li, Y. Cheng, J. Wang, Z. K. Zhou, L. Chen, Nano Letters **23**(23), 10991 (2023).
[23] M. A. Naveed, R. M. H. Bilal, A. A. Rahim, M. A. Baqir, M. M. Ali, Applied Optics **60**(29), 9160 (2021).
[24] M. A. Naveed, J. Kim, I. Javed, M. A. Ansari, J. Seong, Y. Massoud, J. Rho, Advanced Optical Materials **10**(13), 2200196 (2022).
[25] M. Marishwari, V. Subramanian, Z. Ouyang, N. Yogesh, Progress in Electromagnetics Research B **99**(2), 121 (2023).
[26] S. Hao, J. Wang, I. Fanayev, S. Khakhomov, J. Li, Optical Materials Express **13**(1), 247 (2022).
[27] K. T. Cahyani, L. O. Nur, H. H. Ryanu, ALINIER: Journal of Artificial Intelligence and Applications **4**(1), 39 (2023).
[28] W. Gao, F. Chen, W. Yang, Photonics and Nanostructures **63**, 101366 (2025).
[29] X. Fan, Y. Zhu, Z. Su, N. Li, X. Huang, Y. Kang, B. Assouar, Physical Review Applied **19**(3), 034032 (2023).
[30] G. Lee, S. J. Lee, J. Rho, M. Kim, Materials Today Energy **37**, 101387 (2023).
[31] W. Gao, F. Chen, W. Yang, Optics Communications **590**, 132027 (2025).
[32] Y. Li, S. Yang, Q. Lin, S. Li, M. Su, L. Tang, Applied Optics **62**(27), 7139 (2023).
[33] M. Rashki, M. R. Rakhshani, Plasmonics **18**(4), 1351 (2023).
[34] Z. Ding, W. Su, L. A. Ye, Y. Zhou, W. Li, R. Ali, H. Yao, Chinese Optics Letters **22**(6), 063601 (2024).
[35] H. Pakarzadeh, Z. Fatemipanah, U. A. Kumar, Silicon **15**(15), 6655 (2023).
[36] S. K. Patel, A. K. Udayakumar, G. Mahendran, B. Vasudevan, J. Surve, J. Parmar, Scientific Reports **12**(1), 18044 (2022).
[37] K. Chaudhuri, M. Alhabeb, Z. Wang, V. M. Shalaev, Y. Gogotsi, A. Boltasseva, ACS Photonics **5**(3), 1115 (2018).
[38] Y. Jia, T. Wu, G. Wang, J. Jiang, F. Miao, Y. Gao, Nanomaterials **12**(16), 2753 (2022).
[39] M. Abou Houran, L. F. Abdulrazak, M. A. Baqir, M. Saqlain, A. Hassan, International Journal of Thermal Sciences **196**, 108713 (2024).
[40] Y. Pan, Y. Li, F. Chen, S. Cheng, W. Yang, B. Wang, D. Yao, Physical Chemistry Chemical Physics **25**(40), 27586 (2023).
[41] Handbook of optical constants of solids **3**, E. D. Palik ed., Academic Press, 1997.
[42] Z. Jakšić, M. Obradov, D. Tanasković, O. Jakšić, D. Vasiljević Radović, Optical and Quantum Electronics **52**, 1 (2020).
[43] B. Li, Q. Wu, K. Ouyang, F. Li, Y. Li, X. Zhou, J. Wang, Physica B: Condensed Matter **700**, 416935 (2025).
[44] R. Ali, W. Su, M. Ali, N. M. Khan, Diamond and Related Materials **152**, 111986 (2025).
[45] Y. Ren, W. Cui, Z. Li, L. Zhang, Z. Yang, S. Lu, Z. He, Renewable Energy **231**, 120877 (2024).
[46] M. Q. Mehmood, A. R. Shah, M. A. Naveed, N. Mahmood, M. Zubair, Y. Massoud, IEEE Access **11**, 130287 (2023).
[47] Z. Gao, Plasmonics **19**, 1961 (2024).
[48] L. Lei, S. Li, H. Huang, K. Tao, P. Xu, Optics Express **26**(5), 5686 (2018).
[49] Y. Xu, P. Bai, X. Zhou, Y. Akimov, C. E. Png, L. K. Ang, W. Knoll, L. Wu, Advanced Optical Materials **7**(9), 1801433 (2019).
[50] Y. Liu, W. Z. Ma, Y. C. Wu, D. Meng, C. Dou, Y. Y. Cheng, Y. Gu, Optics Communications **542**, 129588 (2023).
[51] J. F. Ruan, Z. Tao, Z. F. Meng, S. M. Pan, Journal of Physics D: Applied Physics **55**(48), 485102 (2022).
[52] R. Li, X. Wang, M. Chen, Catalysts **13**(6), 940 (2023).
[53] Y. Xu, P. Qiu, J. Mao, H. Jile, P. Jiang, Diamond and

Related Materials **132**, 109624 (2023).
[54] Air Mass 1.5 Spectra, American Society for Testing and Materials (ASTM), http://rredc.nrel.gov/solar/spectra/am1.5/
[55] M. Shabani, A. Mir, IEEE Journal of Quantum Electronics **57**(3), 1 (2021).
[56] M. Leipold, COSPAR Colloquia Series **11**, 337 (2001).
[57] M. R. Rana, E. U. Biswas, S. M. Mahmud, S. M. Sahel, S. S. Hassan, M. R. Chowdhury Mahdy, Advanced Engineering Materials **25**(20), 2300438 (2023).

*Corresponding author: chenfang2024@126.com